Application of machine learning to predict the multiaxial strain-sensing response of CNT-polymer composites

Miguel A.S. Matos, Silvestre T. Pinho and Vito L. Tagarielli[1]

Department of Aeronautics, Imperial College London, SW7 2AZ London, UK

Abstract

We present predictive multiscale models of the multiaxial strain-sensing response of conductive CNT-polymer composites. Detailed physically-based finite element (FE) models at the micron scale are used to produce training data for an artificial neural network; the latter is then used, at macroscopic scale, to predict the electro-mechanical response of components of arbitrary shape subject to a non-uniform, multiaxial strain field, allowing savings in computational time of six orders of magnitude. We apply this methodology to explore the application of CNT-polymer composites to the construction of different types of sensors and to damage detection.

Accepted in *Carbon*, February 2019

1 INTRODUCTION

The increasing amount of interest in using CNTs as a filler in multifunctional material systems is due to their great mechanical [1], electrical [2] and thermal [3] properties, allowing to enhance composites applications [4] and to develop multifunctional materials with sensor capabilities [5, 6]. In particular, the piezo-resistive response of CNT-polymer composites can be exploited in strain-sensing applications: upon loading, the applied deformation distorts the conductive paths that the CNTs form within the polymer matrix, resulting in a substantial change of the bulk conductivity of the material [7].

Several authors [8-17] have performed predictions of the strain-sensing response of these materials; however they have considered only the case of loading by uniform strain fields, in most cases in uniaxial stress scenarios. Previous modelling approaches were based on the analysis of micron-sized representative volume elements (RVEs) and as such they are too computationally demanding to be used in the case of real applications, which in general involve macroscopic-sized components subject to non-uniform, multiaxial strain fields.

Tallman and Wang [18] proposed a phenomenological analytical model predicting the sensitivity of conductivity to imposed uniform multiaxial strain fields. This approach is based on percolation probability, which is valid only in the vicinity of the percolation threshold [9,

[1] Corresponding author. E-mail v.tagarielli@imperial.ac.uk

19], and requires several parameters to be determined from comparison to experiments; it was applied to reconstruct a strain field from electrical impedance tomography measurements [20].

The computational cost of physically-based models can be substantially reduced by applications of supervised machine learning [21]. Recently, deep learning has emerged as an attractive tool to reduce model complexity, and artificial neural networks (ANNs) have been successfully used for a variety of applications [22], from pattern recognition and classification [23] to event forecasting or even cancer predictions [24]. Several applications have been in structural analysis [25] and material science, ranging from studies of atomic properties [26] and interatomic potentials [27] to the mechanical properties of several materials [28-31], including those of individual CNTs [32].

This study builds on detailed physically-based models recently developed by the authors [17]. It applies machine learning to achieve model order reduction and to perform, for the first time, predictions of the strain-sensing response of macroscopic complex components made from CNT-polymer composites and subject to arbitrary, non-uniform multiaxial strain fields. The approach does not involve calibration parameters to be determined from complex experiments and it explicitly accounts for quantum tunnelling electron transport at the junction between CNTs [33]. The application of machine learning also allows portability of the electro-mechanical constitutive model, which is of very low computational cost and can be immediately used by relatively inexperienced users.

The structure of the paper is as follows: in Section 2, we summarise the FE models upon which the machine learning exercise builds. In Section 3, we detail the application of machine learning to the problem. In Section 4, we present several applications of the new modelling methodology, before concluding in section 5.

2 MICRO-SCALE FINITE ELEMENT MODELS

The proposed methodology is based on sequentially-coupled electro-mechanical FE simulations that analyse the response of micron-sized material RVEs, predicting the sensitivity of the conductivity tensor of CNT-polymer composites to applied uniform strain fields. These physically-based models, recently proposed by the authors [17], account explicitly for tunnelling conductivity at the junctions between CNTs and perform true predictions, in the sense that they do not necessitate of calibration parameters but only depend on the physical properties of the CNTs and the polymer matrix, as well as on the electron extraction potential at the CNT junctions and on the relative dielectric permittivity of the polymeric matrix. Here we summarise the main features of such models and we refer the reader to [17] for details.

RVEs are constructed by randomly seeding CNTs with a random orientation within a cubic matrix volume of side L_{RVE}, until the desired volume fraction v_{f} is reached (see Fig. 1). CNTs are modelled as arrays of straight segments and have diameter D_{CNT} and length L_{CNT}. Geometric periodicity is enforced at the RVE boundaries and a minimum distance between adjacent CNTs is ensured by identifying all intersections and locally perturbing the CNT segments so that their initial separation distance s is always equal or greater than the van der Waals equilibrium distance of $d_{\mathrm{VDW}} = 0.34$ nm. An example of an RVE is shown in Fig. 1.

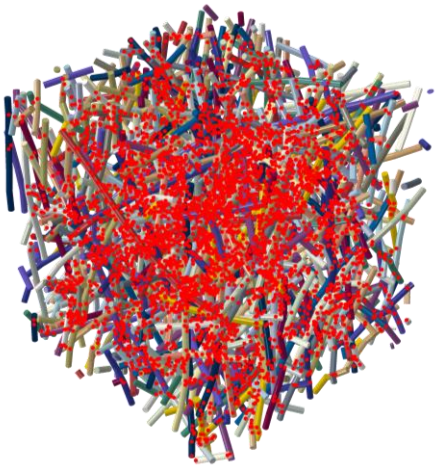

Fig. 1. Example of the RVEs studied by Matos at al. [17] highlighting the contact locations. For visualization purposes, a smaller RVE and shorter CNTs than those described in this study are considered, with 1% volume fraction.

2.1 Mechanical analysis

In the mechanical analysis, the single-wall CNTs are modelled as continuum beams with a hollow circular cross section of wall thickness 0.34 nm [34] – the interlayer thickness of graphene – and discretized using the B31 beam elements of Abaqus Standard [35]. The material behaviour is taken as linear isotropic, with effective material properties obtained from published measurements or atomistic simulations. The polymeric matrix is discretized into a regular grid of 8-noded brick elements (C3D8 of Abaqus) in which the nanotubes are embedded, assuming perfect bonding with the matrix. Mechanical periodic boundary conditions are prescribed at the boundaries, via constraints to appropriate master nodes, whose degrees of freedom correspond to 6 homogenized strain components, while the corresponding reaction forces are related to 6 independent homogenized stress components. Simulations are conducted for different multiaxial homogenised strain cases; the average and spread of the homogenised elastic properties are obtained by a Monte Carlo analysis, by examining 20 different realisations of the material's microstructure.

The mechanical analysis allows determining the change in the separation distance s between each contacting pair of CNTs; this allows computing the sensitivity (S_k^l) of the separation distance (s_k) of each contact junction (k), and in each load case (l), to the load case amplitude A_l, $S_k^l = \partial s_k / \partial A_l$. Each load case is defined as a linear combination of the homogenised principal strain components $\bar{\varepsilon}_i^l = a_i \bar{\varepsilon}_{\mathrm{p_{max}}}$ (an overbar denotes homogenized strains; roman indices will refer to the principal strain directions $i = \mathrm{I, II, III}$); a_i are randomly generated numbers in the range $[-1, +1]$ and $\bar{\varepsilon}_{\mathrm{p_{max}}}$ the maximum considered principal strain.

2.2 Electrical analysis

The same RVEs are used for the electrical analysis, giving the bulk conductivity of the RVEs in different directions. The matrix is discretized by a regular mesh in which the nanotubes, meshed by one-dimensional conductive link elements (DC1D2 of Abaqus), are embedded. The embedding is done by constraining the CNT voltage degrees of freedom (DOFs) to the

corresponding DOFs of the matrix, via linear shape functions. The electrical analysis is performed using a steady-state heat-transfer analysis in Abaqus [35], since this type of analysis has a support for user-defined subroutines; the constitutive equations for electrical and thermal conductivity problems are analogous, as long as the adequate thermal properties are replaced by the electrical equivalents [36]. The polymeric matrix is modelled by DC3D8 8-noded brick elements.

At all contact junctions, defined as minimum-distance segments between distinct nanotubes, of length inferior to $d_{\text{cut-off}} = 4$ nm (as the junction conductivity is negligible at this distance), a user-defined element that models the quantum tunnelling transport is applied (referred to as "junction element"). This is integrated into a UEL subroutine in Abaqus [37] that reproduces the fluctuation-induced tunnelling electron transport between adjacent CNTs, modelled using Simmons's generalized formula [33] as described in [17]. The current that flows through these junction elements therefore depends on the CNT work fraction (extraction potential of one electron), on the permittivity ϵ of the polymeric matrix and on the separation distance between the adjacent CNTs. For each tunnelling element (k), the separation distance s_k is defined as the maximum value between the minimum separation $s_{\text{min}} = 0.25$ nm (as determined in [38]) and the sum of the initial distance s_{k_0} with the additional separation due to the imposed deformation:

$$s_k = \max\{s_{\text{min}}, s_{k_0} + S_k^l A_l\}. \tag{1}$$

The junction elements have 2 physical nodes and 3 DOFs: the electrical potential at the two physical nodes and a 3rd DOF corresponding to the load case amplitude A_l, which is prescribed as the DOF of an additional master node, shared by all the junctions. Fig. 2 illustrates this schematically.

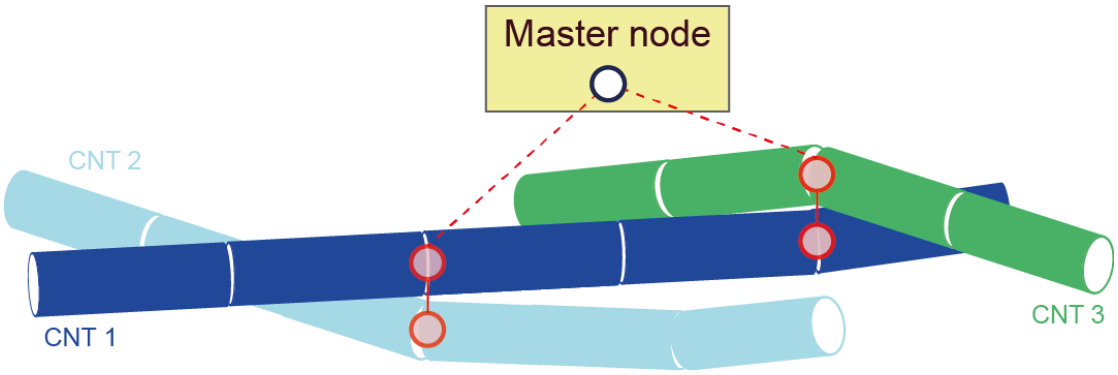

Fig. 2. Illustration of the physical nodes and the master node of junction elements.

Electric periodic boundary conditions are prescribed at the RVE boundaries, allowing imposing uniaxial homogenised electric fields (or potential differences) along each of the 3 Cartesian directions, by adjusting the 3 DOFs of a master node. The reaction flux components at the same node represent the current that flows through the RVE in the 3 Cartesian directions, from which the conductivity tensor is computed. An electric field is applied, at each value of the imposed strain field, in each of the 3 Cartesian directions, allowing computation of the conductivity tensor as function of the imposed homogenized strain field. We note that since the RVEs are isotropic, the conductivity tensor is diagonal (i.e. $\kappa_{ij} = 0$ for $i \neq j$).

3 APPLICATION OF MACHINE LEARNING

The models described in Section 2 are used to produce extensive data for training of an artificial neural network able to predict the material conductivity tensor as a function of the applied multiaxial state of strain. An ANN consists of a set of sequentially-ordered layers, with each layer (j) comprising a set of neurons; each neuron (i) in layer (j) contains a variable storing a real value $v_i^{(j)}$, which is a linear combination of the values of the prior layer, activated by a non-linear function f_{A} [22], that is

$$v_i^{(j)} = f_{\mathrm{A}}\left(w_{ik}^{(j)} v_k^{(j-1)} + b_i^{(j)}\right) \tag{2}$$

where $\mathbf{w}^{(j)}$ and $\mathbf{b}^{(j)}$ are the weight matrix and bias array of the j-th layer. Einstein convention on summation over repeated indices applies.

The layer of inputs consists of the imposed homogenised principal strains $\{\bar{\varepsilon}_{\mathrm{I}}, \bar{\varepsilon}_{\mathrm{II}}, \bar{\varepsilon}_{\mathrm{III}}\}$, while the layer of outputs contains the changes of resistance in the 3 principal directions, normalized by the initial value R_0, $\{\Delta R_{\mathrm{I}}/R_0, \Delta R_{\mathrm{II}}/R_0, \Delta R_{\mathrm{III}}/R_0\}$; this vector allows calculating the homogenised conductivity tensor, written in principal strain space. For each principal component i, the relation between the local deformed κ_i and initial κ_0 conductivities is

$$\kappa_i = \frac{\kappa_0}{\frac{\Delta R_i}{R_0} + 1} \tag{3}$$

For the problem under investigation, dimensional analysis dictates that such non-dimensional changes in resistance depend on the principal strains $\{\varepsilon_{\mathrm{I}}, \varepsilon_{\mathrm{II}}, \varepsilon_{\mathrm{III}}\}$ and on the following set of non-dimensional parameters Π_i:

$$\Pi_1 = \frac{E_{\mathrm{CNT}}}{E_{\mathrm{mat}}};\ \Pi_2 = \nu_{\mathrm{mat}};\ \Pi_3 = \frac{\kappa_{\mathrm{CNT}}}{\kappa_{\mathrm{mat}}};\ \Pi_4 = \frac{L_{\mathrm{CNT}}}{D_{\mathrm{CNT}}};\ \Pi_5 = \frac{\kappa_{\mathrm{CNT}} h}{\epsilon \varphi_0}, \Pi_6 = v_{\mathrm{f}} \tag{4}$$

where the subscript CNT and mat correspond to the nanotube and matrix properties, respectively. E represents the elastic modulus, ν the Poisson's ratio, κ the electrical conductivity, φ_0 the tunnelling junction potential barrier (taken as the CNT work fraction), ϵ the matrix permittivity, h Plank's constant and v_{f} the nanotube volume fraction.

Relevant physical material properties are presented in Table I; in addition, the tunnelling junctions had a work fraction of $\varphi_0 = 4.95$ eV [39] and a permittivity of $3.98 \times \epsilon_0$, where ϵ_0 is the vacuum permittivity (representative of an epoxy matrix). A volume fraction of $v_{\mathrm{f}} = 1.0\%$ was chosen, driven by the fact that this is just above the percolation threshold, and in this region the materials are expected to display the most prominent strain-sensing response [17]. These properties are compatible with non-dimensional parameters with values: $\Pi_1 = 10^3, \Pi_2 = 0.35, \Pi_3 = 10^{10}, \Pi_4 = 10^2, \Pi_5 = 0.2369, \Pi_6 = 0.01$, and results are valid only for this choice.

Material	Elastic modulus (E)	Poisson's ratio (ν)	Electrical conductivity (κ)	Diameter (D_{CNT})	Length (L_{CNT})
CNT	1.0 TPa	–	10^4 S/m	50 nm	5 μm
Epoxy	1.0 GPa	0.35	10^{-6} S/m	–	–

Table I. Relevant material properties and CNT geometry [13].

Following a preliminary RVE size and mesh convergence study, RVEs with $L_{\mathrm{RVE}} = 2.0 \times L_{\mathrm{CNT}}$ were simulated, resulting in models with approximately 650000 and 350000 DOFs for the mechanical and electrical simulations, respectively. For the chosen volume fraction, the homogenised conductivity of the undeformed composite was $2.187\ \mathrm{S/m}$, the homogenised elastic modulus was $2.944\ \mathrm{GPa}$ and the homogenised Poisson's ratio 0.3375. These homogenised elastic properties, independent of strain, were used in the coupled electromechanical simulations of the response of macroscopic components, to define the homogenised elastic isotropic mechanical behaviour of the material.

The sequentially-coupled simulation technique illustrated in [17] was used to simulate the response of the RVEs to imposed uniform multiaxial strain states as well as potential differences, to generate training data for the machine learning application. The imposed strain amplitudes were as large as 1% and the loading cases consisted of pseudo-random combinations of the 3 imposed principal strains. An electric field of $0.01\mathrm{V/nm}$ was imposed on opposite boundaries of the RVEs, along each of the 3 Cartesian directions. We note in passing that the tunnelling conductivity at the junctions between adjacent CNTs is, strictly, non-linear in potential difference [33]; however, a preliminary study showed that this non-linearity is negligible in the range $0.01 - 0.1\ \mathrm{V/nm}$ and we therefore consider the conductivity tensor independent of applied voltage in this study.

The choice of the number of hidden layers and of the number of neurons in each layer was the result of a trial and error procedure; the optimal network had 2 hidden layers, each with 3 neurons, as sketched in Fig. 3. The training sets consisted of 15000 pairs of inputs and outputs vectors; 14500 pairs were used to train the ANN and the remaining 500 to determine the validation accuracy. The validation set is selected from distinct load cases, guaranteeing that the ratio between strain components is unseen by the network during training.

Since the change in resistivity scales approximately exponentially with strain [17], training of the ANN was facilitated by redefining the 3 outputs as $\log_{10}\left(c + \frac{\Delta R_i}{R_0}\right)$, where c is a positive real number larger than the maximum absolute negative value (set to $c = 0.15$) which keeps the argument of the logarithm positive. A sigmoid function was chosen as the activation of the inner layers, $f_{\mathrm{A}}(x) = (1 + e^{-x})^{-1}$, and identity function (i.e. no activation) was used for the output layer.

The network was built and trained using TensorFlow [40], which allowed determining the optimal weight matrices and bias arrays $\mathbf{w}^{(j)}$ and $\mathbf{b}^{(j)}$ to minimise the mean square error between the predictions of FE simulations and those of the ANN; such optimisation was conducted via backpropagation, using the Adam algorithm [41]. A small L2 regularization, with a value of $\lambda = 10^{-5}$, was used to avoid overfitting. The resulting optimized network reached training and validation accuracies of 99.72% and a 99.68%, respectively, after 1000 epochs (forward and backward passes of all the data, shuffled and divided in batches of 8 pairs of training sets). Incidentally, we note that we repeated the training for an 80:20 ratio of training to validation dataset size (as such ratio is widely used in machine learning) and, for the same network and number of epochs, we obtained similar training and validation accuracies (of 99.648% and 99.690%, respectively).

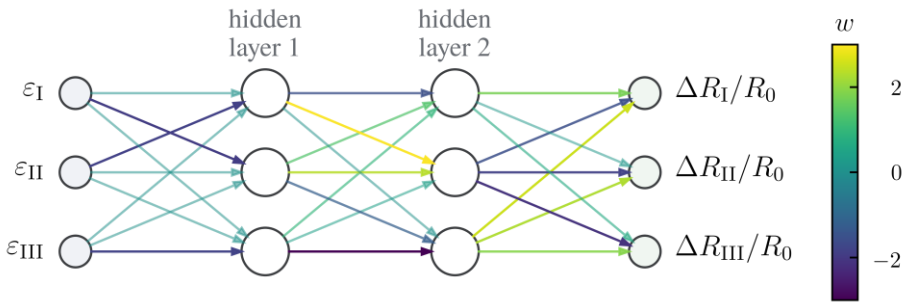

Fig. 3. Schematics of the optimized ANN and of respective weights.

To illustrate explicitly the accuracy of the optimized ANN, in Fig. 4 we present predictions of strain-sensing for loading in uniform uniaxial stress and uniform uniaxial strain, examined in detail in [17]. The curves show the change in non-dimensional resistance in direction 1 as a function of the imposed strain in the same direction. Such predictions correspond to an applied potential difference in direction 1, and two sets of predictions are shown: the first set is obtained from a detailed sequentially-coupled analysis of the mechanical and electrical FE models described above, while the second set represents predictions of the optimised ANN. Good agreement between the two sets is clear, for both tensile and compressive imposed macroscopic strain. We note that none of these 2 load cases was part of the training dataset for the ANN. Each FE simulation required around 3.5h of CPU time (and 20 simulations were necessary for the Monte Carlo analysis), while the ANN allowed to reproduce the same predictions in less than 0.2s of CPU time; this corresponds to a saving in computational time of more than 6 orders of magnitude.

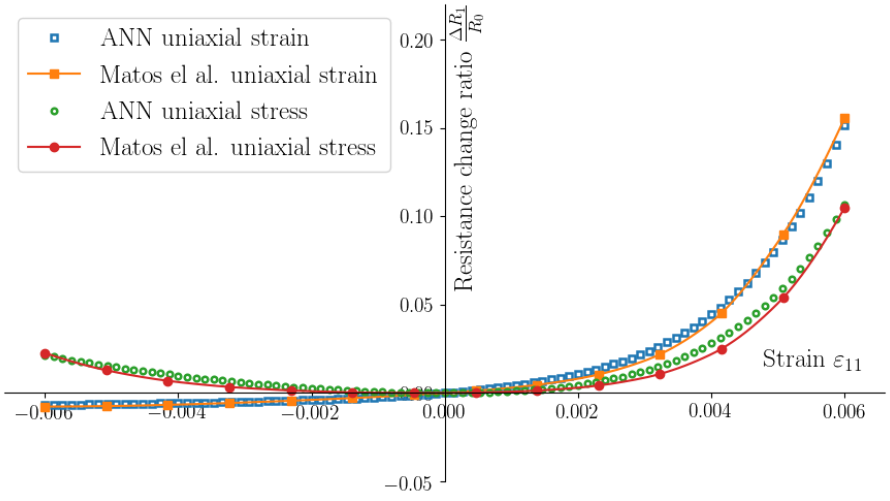

Fig. 4. Change in resistance as a function of strain, as predicted by the FE simulations and the ANN, showing the validation of the ANN for uniaxial strain and stress load cases.

The optimized network was used to construct a FORTRAN function to be used in simulations of macroscopic components in Abaqus [35]; such function provides the vector **Y** containing the 3 outputs as a function of the vector **X** containing the 3 inputs, as follows

$$\mathbf{Y} = \mathbf{b}^{(3)} + \mathbf{w}^{(3)} \times f_{\mathrm{A}}\left(\mathbf{b}^{(2)} + \mathbf{w}^{(2)} \times f_{\mathrm{A}}\left(\mathbf{b}^{(1)} + \mathbf{w}^{(1)}\mathbf{X}\right)\right) \tag{5}$$

$$\mathbf{w}^{(1)} = \begin{bmatrix} -1.0858 \times 10^{-1} & -1.8058 & -1.0533 \times 10^{-1} \\ -1.9124 & -1.0525 \times 10^{-1} & -8.7031 \times 10^{-2} \\ -7.9171 \times 10^{-2} & -7.9752 \times 10^{-2} & -1.7554 \end{bmatrix}, \mathbf{b}^{(1)} = \begin{Bmatrix} 3.6989 \\ 3.7150 \\ 3.5303 \end{Bmatrix} \tag{6}$$

$$\mathbf{w}^{(2)} = \begin{bmatrix} -1.4643 & 1.1072 & 7.1857 \times 10^{-1} \\ 2.5401 & 1.9233 & 2.4055 \times 10^{-1} \\ -9.6173 \times 10^{-3} & -1.1108 & -2.8318 \end{bmatrix}, \mathbf{b}^{(2)} = \begin{Bmatrix} -1.6504 \\ -3.3004 \\ 2.5294 \end{Bmatrix} \tag{7}$$

$$\mathbf{w}^{(3)} = \begin{bmatrix} 1.4034 & -1.4799 & 1.9688 \\ 6.5250 \times 10^{-2} & -1.7152 & 1.7605 \\ 4.4283 \times 10^{-1} & -1.9572 & 1.4402 \end{bmatrix}, \mathbf{b}^{(3)} = \begin{Bmatrix} -3.9414 \\ 1.1168 \\ 2.9051 \end{Bmatrix} \times 10^{-1} \tag{8}$$

where the input vector is related to the normalized (considering the average and standard deviation of training data) principal strain components $\varepsilon_i : (i = \mathrm{I}, \mathrm{II}, \mathrm{III})$ by

$$\mathbf{X} = \left\{ \frac{\varepsilon_i - (-2.5868 \times 10^{-5})}{3.4109 \times 10^{-3}} \right\} \tag{9}$$

and the final resistance along each of the principal directions given by

$$\frac{\Delta R_i}{R_0} = -0.15 + 10^{Y_i} \tag{10}$$

The simulations on macroscopic components were steady-state coupled temperature-displacement analyses, where the analogy of the thermal and electrical physical problems was exploited via appropriate substitutions of variables. The CNT-polymer composite material was modelled by 8-noded thermally-coupled brick elements, with trilinear displacement and temperature (C3D8T). A user-defined field (USDFLD subroutine of Abaqus [37]) was used to read and store the Cartesian strain components at each integration point, at the start of each solution increment. The electrical constitutive behaviour was specified through a user defined material (UMATHT subroutine of Abaqus [37]), which contained the FORTRAN function constructed by the ANN (eq. (5)), providing the conductivity tensor (in a principal strain reference system) as a function of the imposed principal strain. This tensor was then appropriately rotated to obtain the conductivity in a global Cartesian reference system.

In the following section, we present different applications of the proposed modelling methodology to problems of practical interest.

4 APPLICATIONS

4.1 Measurements of the strain-sensing response of materials

As a first application we consider the tensile loading of the flat dog bone specimen in Fig. 5, dimensioned according to ASTM D638-02 [42]. A specimen of this geometry, or similar, may be used to conduct measurements of the strain-sensing response of a CNT-polymer composite. Such measurement would typically occur by placing 2 electrodes at opposite ends of the specimen's end tabs, injecting a known current into the specimen by connection to a constant current source; a potential difference can then be measured by the same electrodes (2-probe set-up) or by an additional pair of electrodes at different locations along the specimen (4-probe set-up). Placing voltage-measuring electrodes at the end of the specimen, in a 2-probe configuration, may be convenient as this allows sampling the average electrical potential across the specimen thickness; a 4-probe set-up however is expected to be more accurate, as the electrodes measuring the potential difference may be placed at the ends of the gauge section, in which the strain field is uniform. For the 2 types of measurements to coincide, the material conductivity should change uniformly along the specimen; however, this is not the case, due to the gradients in strain field outside the gauge portion. The models presented in this paper allow quantifying this, assessing whether the effects of strain gradients are negligible in this type of measurements.

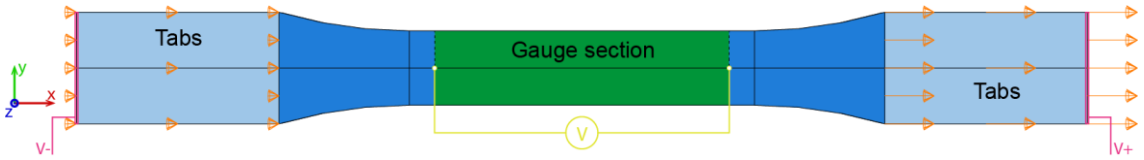

Fig. 5. Geometry of the tensile specimen and sketch of the prescribed boundary conditions, including locations of the voltage probes.

The electro-mechanical response of the specimen was simulated, imposing an axial strain of up to 1% in the gauge section; this was achieved by fully constraining one of the end-tabs while imposing an axial displacement on the opposite tab. The electrical constitutive model of each finite element was provided by the ANN (eq. (5)), as described above. Fig. 6 shows the axial strain and axial conductivity fields at an imposed gauge strain of 1%. Clearly, the conductivity along the specimen is non-uniform and its value in the gauge portion is approximately 50% of the value at the undeformed end tabs, suggesting that a 4-probe set-up should yield much more accurate measurements than a 2-probe set-up.

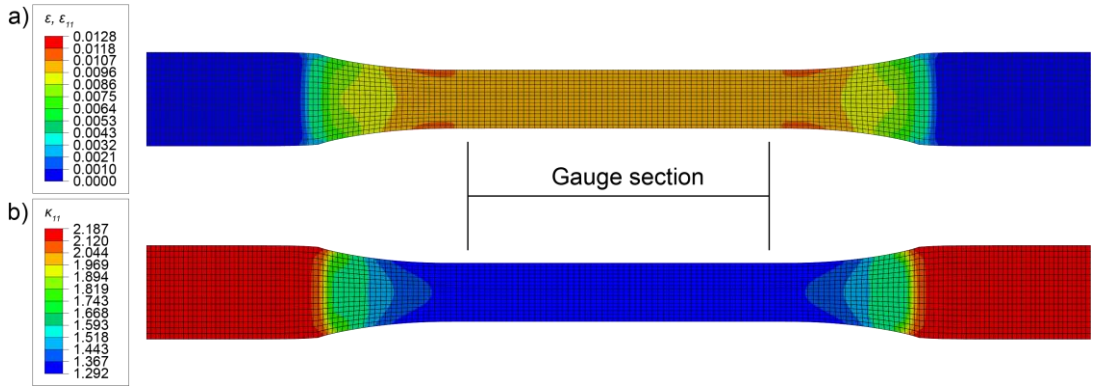

Fig. 6. Contours of the a) axial strain and b) axial conductivity fields when a strain of 1% acts in the gauge portion.

Fig. 7 shows the measured changes in resistance for the 2-probe and 4-probe set-ups, compared with the expected resistance versus strain history predicted in the case of uniaxial stress (by the ANN). Clearly the 4-probe method, with voltage electrodes placed at the ends of the gauge portion, can capture the correct response, while the 2-probe set-up underestimates the sensitivity of conductivity to strain. On the other hand, the electrodes measuring voltage in a 4-probe set-up can only contact the specimen's surface, and if a boundary layer of low CNT concentration exists at the surface, this can affect the measurements substantially. Our simulations show that the electrical potential and current density at the ends of the gauge portion are, to a very good approximation, uniform in the cross-section (considering a perfect CNT dispersion); this ensures that the use of surface electrodes is appropriate. These considerations, and the high variability of the measurements reported in the literature on similar materials, suggest that extreme care must be taken in interpreting this type of measurements.

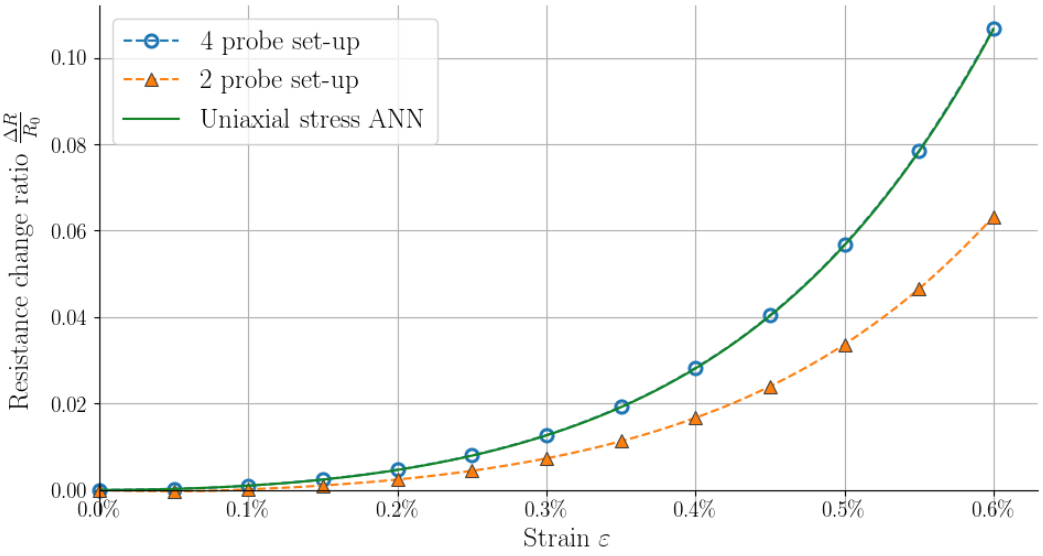

Fig. 7. Relative change in resistance as a function of axial strain in the gauge portion of the tensile specimen.

4.2 Damage detection

The second application explores the suitability of CNT-polymer composites for damage detection applications; thin layers of these materials may be adhered to safety critical structures, e.g. in aeronautical applications, to monitor strain and simultaneously detect possible damage. Suppose that a strip of CNT-polymer composite is adhered to a structure of similar Poisson's ratio and mainly loaded in uniaxial tension, and that this structure is subject to (e.g.) impact damage. Damage may remove some material, which we idealise as the presence of a hole in the strip and structure.

To investigate this scenario, we simulate the electro-mechanical response of a material strip with a central hole, loaded in uniaxial tension. The strip has a length to width ratio $L/W = 4$ and a central hole of diameter $0.2\ W$, as shown in Fig. 8 together with the prescribed boundary conditions (constrained displacement at the left boundary and prescribed longitudinal displacement on the opposite side). The length and width of the strip represents the spacing of the probes at which the electrical resistance is sampled in the application considered. The axial strain and axial conductivity fields at an imposed displacement of $0.006 \times L$ are shown in Fig. 8.

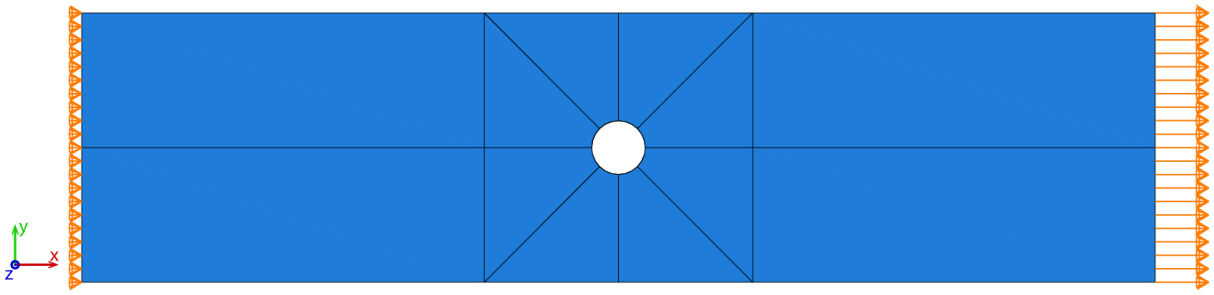

Fig. 8. Geometry and boundary conditions for a rectangular material strip with a central hole.

The resistance is computed as the electric potential difference across the specimen's ends, divided by the current that flows through it. The presence of the hole induces an increase in the resistance of the unstrained (R_0) strip of 1.65%, suggesting that the material under investigation could comfortably detect the occurrence of damage. We note however that the hole diameter chosen here corresponds to a relatively very large damage, and that smaller damage will be harder to detect. In a real damage detection application, length and width should be optimised to maximise the sensitivity to damage, considering the range of damage sizes that are possible or expected. The normalized change in resistance as a function of the applied strain is plotted in Fig. 10 and compared to the case of an identical strip with the hole absent. Clearly, the normalized change in resistance with strain is not significantly affected by the presence of the hole, suggesting that the material strip would continue to act effectively as a strain sensor, even in the case that damage occurs, noting that the undeformed resistance value R_0 is different.

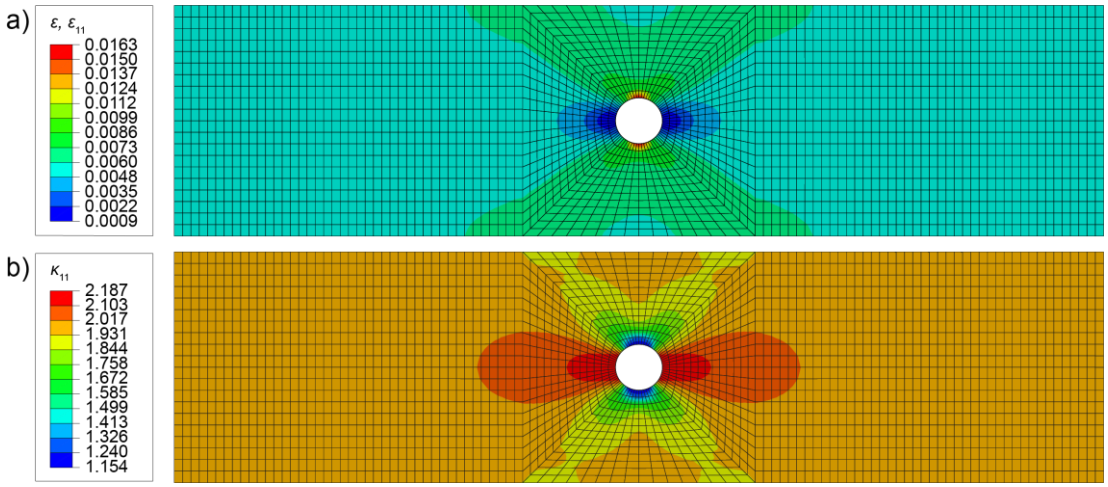

Fig. 9. Contours of the axial strain (a) and axial conductivity (b) fields at an imposed displacement of $0.006 \times L$.

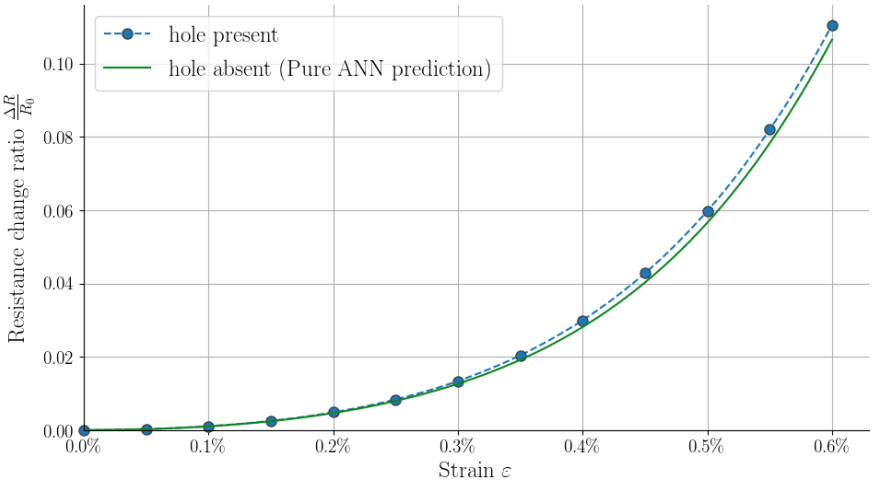

Fig. 10. Normalised change in resistance of the strip as a function of the applied strain, revealing the minor effect of the hole on the strain-sensing response.

4.3 Strain-sensing in bending

We now use the capabilities of the proposed multiscale model to explore the possibility of using bending-governed structures in strain-sensing application, e.g. for the construction of low-cost sensors. Since bending deformation induces a normal strain field which is antisymmetric with respect to the neutral plane, it can be logical to conjecture that strain-sensing capabilities of CNT-polymer composites may be reduced in bending, compared to the case of uniform tension or compression, as the reduction in resistivity in zones of compressive strain may be compensated by an increase in zones of tensile strain. However, the strain-sensing response of these materials is asymmetric (as shown for example in Fig. 4) and therefore a quantitative analysis is needed.

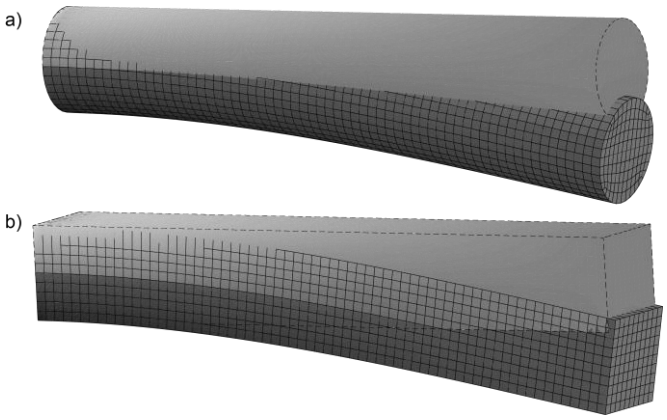

Fig. 11. Initial and deformed shapes of the a) circular and b) square cantilever beams.

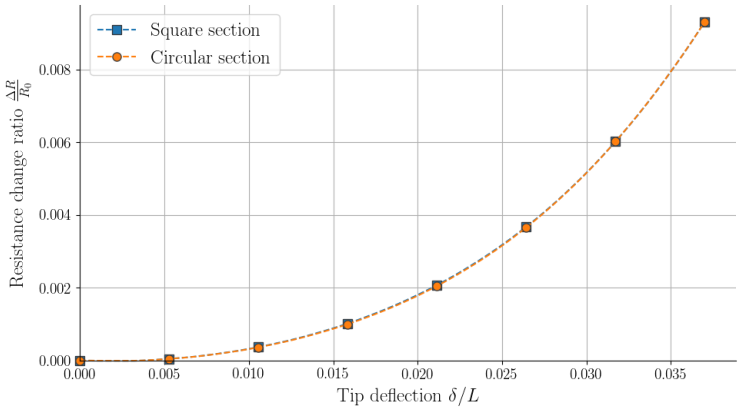

Fig. 12. Change in resistance of the square and circular cantilever beams as a function of the normalised tip deflection.

Here we analyse the change in axial resistance of two prismatic cantilevers loaded at the tip by a transverse displacement. The beams have identical length L and flexural rigidity EI (I represents the second moment of area of the cross-section) and two different cross-sectional shapes, as shown in Fig. 11: circular and square. The aspect ratio of the circular beam was chosen as $L/D = 6$. The beams are built-in at one end and a transverse displacement is applied at the opposite end, such to impose a maximum absolute principal strain of 1% for both cases (as this is the limit of the training range of the ANN). Beams are modelled by 3D brick thermo-elastic elements. An electric voltage is applied at the 2 ends and the resistance is calculated by measurements of flowing current.

Fig. 12 shows the predicted variation of resistance with the applied tip deflection. Both cantilevers display a similar response, with the square section displaying a slightly superior sensitivity of the resistance to deformation (with a maximum difference of 2%). As expected, the relative change of resistance is considerably smaller than that observed in the applications considered previously; however, this is still substantial, even for these relatively slender structures, and this suggests that short, stiff cantilevers of optimal cross-sectional shapes could be designed to maximise the sensitivity of their resistance to bending deflection. Alternatives may include having two separate strips of this material on the superior and inferior parts of the beam with two distinct measurement channels. This design is not pursued here for the sake of brevity; however, the interested reader may make direct use of eq. (5) and simple analytical models to pursue this.

4.4 Plates as touch sensors

Finally, we use the new model to analyse the strain-sensing response of plates loaded transversally, to assess their contact-detection capability. We consider a square plate as in Fig. 13, with a prescribed voltage difference applied at two opposite sides of the square. The thickness is 1/10 of the width, and the plate is transversely loaded by a non-conductive rigid, hemispherical indenter of radius equal to the thickness. Two different sets of boundary conditions are considered: (i) the plate is fully clamped at its periphery, corresponding to a bending response (Fig. 13a), and (ii) the plate is supported by a rigid substrate, resulting in an indentation loading (Fig. 13b). Contact between plate and indenter is modelled as frictionless, using a surface-to-surface discretization.

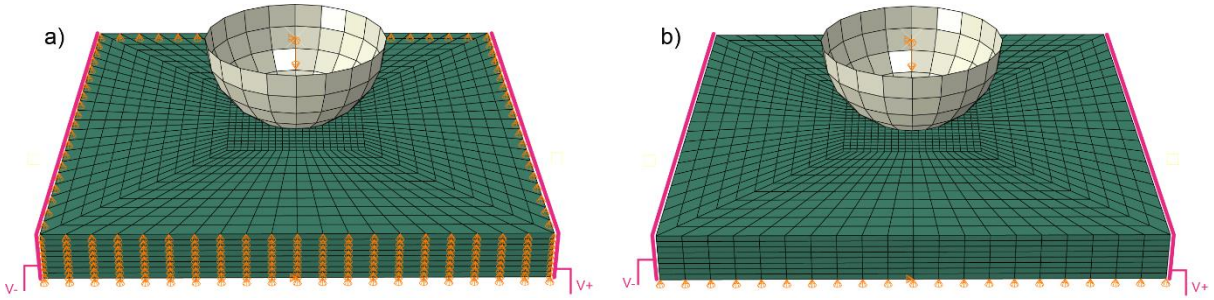

Fig. 13. FE model for transverse plate loading. (a) Plate bending and (b) Plate indentation.

The measured change in resistance is plotted in Fig. 14a as a function of the normalised indenter displacement. The range of indentation depth in this figure extends to $\delta/t = 0.01$, where t is the plate thickness and δ the indentation depth. At this value of indentation the local maximum absolute principal strain is inferior to 1% for both plate bending and plate indentation. In both cases, the localized compressive deformation under the indenter initially decreases the measured resistance. With increased indenter displacement, the reduction in resistance caused by this compressive through-thickness deformation is balanced by the relatively large in-plane tensile strains; the net result is a non-monotonic strain-sensing response. This type of response, indeed, was measured in the experiments on tactile sensors made from carbon nanofibers and a polyurethane matrix, presented in [43]. We note that the magnitude of the change in resistance is quite small, corresponding to a small gauge factor, in this range of displacement, for potential sensors exploiting this type of loading (Fig. 14a).

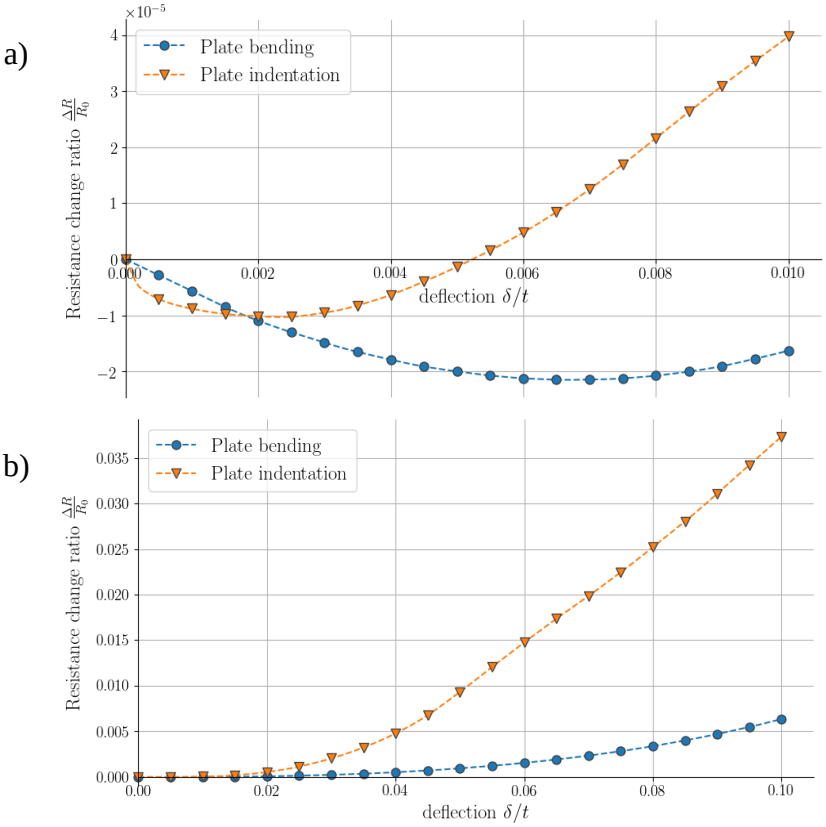

Fig. 14. Normalized change in resistance with the deflection of the contact point δ, normalized by the plate thickness t, until a deflection value of 1% (a) and 10% (b).

If the maximum displacement of the indenter is increased by an order of magnitude, $\delta / t = 0.1$, as shown in Fig. 14b, in both loading conditions the plates display a high change in resistance for indenter displacements greater than approximately 2% of the plate thickness. Fig. 14b also shows that the resulting sensor would be more effective in the case of plate indentation. We note however that these predictions correspond to local strain components higher than 1% and therefore outside the range of training of the ANN used in the simulations; consequently the ANN is extrapolating the material behaviour and for this reason our confidence in these specific predictions is low, and the simulations should be repeated after training of the ANN in a wider strain range, which is not pursued here. We note that for $\delta / t = 0.01$ the local maximum absolute principal strains are of order -13% and 3% for the case of plate indentation and plate bending, respectively. However this large strains are affecting only a very small volume of the material, compared to the volume of the plates, and therefore the error in the predictions is probably also small.

5 CONCLUSIONS

We have presented a physically-based multiscale simulation methodology to predict the strain-sensing response of CNT-polymer composites subject to a non-uniform, multiaxial strain field. The approach involved using detailed FE simulations of RVEs at the micron scale to train an artificial neural network to reproduce, at low computational cost, the electro-mechanical constitutive response at macroscopic scale, in presence of non-uniform multiaxial strain fields. This modelling methodology was implemented in Abaqus and allowed savings in computational time of more than 6 orders of magnitude. Analysis of an RVE of size 1 μm to predict each pair of conductivity-strain takes approximately 3.5h of CPU time (to be multiplied by 20 realizations); the optimised neural network provides the same predictions in less than 0.25s. Clearly this approach enables simulations at the macro-scale which cannot be pursued by explicit modelling of the microstructure. The application of machine learning allows effective packaging of the constitutive information, which is provided to the interested reader via eq. (5), valid for a maximum principal strain not exceeding 1%.

The modelling approach enabled simulations never appeared in the published literature and allowed us to explore realistic applications of CNT-polymer composites. The main practical conclusions drawn from these application studies are:

- Measurements of the strain-sensing response of CNT-polymer composites should be conducted via a 4-probe set-up; if a standard tensile specimen is used, the use of surface electrodes in the experiments is sufficiently adequate.
- The materials under investigation are suitable for applications in structural health monitoring and damage detection; they can be simultaneously used for strain monitoring and their sensitivity to strain is only mildly affected by the occurrence of damage.
- CNT-polymer composites can be used to construct low-cost sensors operating in bending mode, as well as touch sensors operating in indentation mode.

The model developed in this paper enables optimisation of the geometry of sensors to pursue designs of low cost and maximum sensitivity. We leave this as a topic for future studies.

ACKNOWLEDGEMENTS

This project was funded by the European Union's Horizon 2020 research and innovation program, under the Marie Skłodowska-Curie Grant Agreement no. 642890 (http://thelink-project.eu).

REFERENCES

[1] J.N. Coleman, U. Khan, Y.K. Gun'ko, Mechanical reinforcement of polymers using carbon nanotubes, Advanced Materials 18(6) (2006) 689-706.
[2] W. Bauhofer, J.Z. Kovacs, A review and analysis of electrical percolation in carbon nanotube polymer composites, Compos Sci Technol 69(10) (2009) 1486-1498.
[3] Z.D. Han, A. Fina, Thermal conductivity of carbon nanotubes and their polymer nanocomposites: A review, Prog Polym Sci 36(7) (2011) 914-944.
[4] A. Paipetis, V. Kostopoulos, Carbon Nanotube Enhanced Aerospace Composite Materials: A New Generation of Multifunctional Hybrid Structural Composites, Springer Netherlands 2012.
[5] D.D.L. Chung, Carbon materials for structural self-sensing, electromagnetic shielding and thermal interfacing, Carbon 50(9) (2012) 3342-3353.
[6] R.H. Baughman, A.A. Zakhidov, W.A. de Heer, Carbon nanotubes - the route toward applications, Science 297(5582) (2002) 787-792.
[7] G.T. Pham, Y.B. Park, Z. Liang, C. Zhang, B. Wang, Processing and modeling of conductive thermoplastic/carbon nanotube films for strain sensing, Compos Part B-Eng 39(1) (2008) 209-216.
[8] Alamusi, Y.L. Liu, N. Hu, Numerical Simulations on Piezoresistivity of CNT/Polymer Based Nanocomposites, Cmc-Comput Mater Con 20(2) (2010) 101-117.
[9] D. Stauffer, A. Aharony, Introduction To Percolation Theory, Taylor & Francis2003.
[10] M.H.G. Wichmann, S.T. Buschhorn, J. Gehrmann, K. Schulte, Piezoresistive response of epoxy composites with carbon nanoparticles under tensile load, Phys Rev B 80(24) (2009) 8.
[11] Y. Kuronuma, T. Takeda, Y. Shindo, F. Narita, Z.J. Wei, Electrical resistance-based strain sensing in carbon nanotube/polymer composites under tension: Analytical modeling and experiments, Compos Sci Technol 72(14) (2012) 1678-1682.
[12] B. De Vivo, P. Lamberti, G. Spinelli, V. Tucci, L. Vertuccio, V. Vittoria, Simulation and experimental characterization of polymer/carbon nanotubes composites for strain sensor applications, Journal of Applied Physics 116(5) (2014) 054307.
[13] N. Hu, Y. Karube, C. Yan, Z. Masuda, H. Fukunaga, Tunneling effect in a polymer/carbon nanotube nanocomposite strain sensor, Acta Mater 56(13) (2008) 2929-2936.
[14] S. Gong, Z.H. Zhu, On the mechanism of piezoresistivity of carbon nanotube polymer composites, Polymer 55(16) (2014) 4136-4149.
[15] M. Taya, W.J. Kim, K. Ono, Piezoresistivity of a short fiber/elastomer matrix composite, Mech Mater 28(1-4) (1998) 53-59.
[16] F. Panozzo, M. Zappalorto, M. Quaresimin, Analytical model for the prediction of the piezoresistive behavior of CNT modified polymers, Compos Part B-Eng 109 (2017) 53-63.
[17] M.A.S. Matos, V.L. Tagarielli, P.M. Baiz-Villafranca, S.T. Pinho, Predictions of the electro-mechanical response of conductive CNT-polymer composites, J Mech Phys Solids 114 (2018) 84-96.
[18] T. Tallman, K.W. Wang, An arbitrary strains carbon nanotube composite piezoresistivity model for finite element integration, Appl Phys Lett 102(1) (2013) 4.
[19] M. Sahimi, Applications Of Percolation Theory, Taylor \& Francis2003.

[20] H. Hassan, F. Semperlotti, K.W. Wang, T.N. Tallman, Enhanced imaging of piezoresistive nanocomposites through the incorporation of nonlocal conductivity changes in electrical impedance tomography, J Intel Mat Syst Str 29(9) (2018) 1850-1861.
[21] T.M.A.G.K.R. Ramprasad, Machine Learning in Materials Science: Recent Progress and Emerging Applications, Reviews in Computational Chemistry 29(1) (2016) 186-273.
[22] I. Goodfellow, Y. Bengio, A. Courville, Deep Learning, The MIT Press2016.
[23] K.M. He, X.Y. Zhang, S.Q. Ren, J. Sun, Deep Residual Learning for Image Recognition, Proc Cvpr Ieee (2016) 770-778.
[24] J.M. Jerez, I. Molina, P.J. Garcia-Laencina, E. Alba, N. Ribelles, M. Martin, et al., Missing data imputation using statistical and machine learning methods in a real breast cancer problem, Artif Intell Med 50(2) (2010) 105-15.
[25] Z. Waszczyszyn, L. Ziemiański, Neural networks in mechanics of structures and materials – new results and prospects of applications, Computers & Structures 79(22) (2001) 2261-2276.
[26] A.P. Bartok, S. De, C. Poelking, N. Bernstein, J.R. Kermode, G. Csanyi, et al., Machine learning unifies the modeling of materials and molecules, Sci Adv 3(12) (2017) e1701816.
[27] V.L. Deringer, G. Csanyi, Machine learning based interatomic potential for amorphous carbon, Phys Rev B 95(9) (2017) 15.
[28] S. Malinov, W. Sha, Application of artificial neural networks for modelling correlations in titanium alloys, Mat Sci Eng a-Struct 365(1-2) (2004) 202-211.
[29] S. Chatterjee, M. Murugananth, H. Bhadeshia, delta TRIP steel, Mater Sci Tech-Lond 23(7) (2007) 819-827.
[30] G.C. Gardner, M.E. O'Leary, S. Hansen, J.Q. Sun, Neural networks for prediction of acoustical properties of polyurethane foams, Appl. Acoust. 64(2) (2003) 229-242.
[31] L. Ward, A. Agrawal, A. Choudhary, C. Wolverton, A general-purpose machine learning framework for predicting properties of inorganic materials, npj Comput. Mater. 2(1) (2016).
[32] V. Papadopoulos, G. Soimiris, D.G. Giovanis, M. Papadrakakis, A neural network-based surrogate model for carbon nanotubes with geometric nonlinearities, Comput Method Appl M 328 (2018) 411-430.
[33] J.G. Simmons, Generalized Formula for the Electric Tunnel Effect between Similar Electrodes Separated by a Thin Insulating Film, Journal of Applied Physics 34(6) (1963) 1793.
[34] G.M. Odegard, T.S. Gates, L.M. Nicholson, K.E. Wise, Equivalent-continuum modeling of nano-structured materials, Compos Sci Technol 62(14) (2002) 1869-1880.
[35] D.S. Simulia, Abaqus 2018 Documentation, 2018.
[36] J.N. Reddy, An Introduction To The Finite Element Method, McGraw-Hill2006.
[37] D.S. Simulia, Abaqus User Subroutines Guide, 2018.
[38] Y.G. Yoon, M.S.C. Mazzoni, H.J. Choi, J. Ihm, S.G. Louie, Structural deformation and intertube conductance of crossed carbon nanotube junctions, Physical Review Letters 86(4) (2001) 688-691.
[39] M. Shiraishi, M. Ata, Work function of carbon nanotubes, Carbon 39(12) (2001) 1913-1917.
[40] M. Abadi, P. Barham, J. Chen, Z. Chen, A. Davis, J. Dean, et al., TensorFlow: a system for large-scale machine learning, Proceedings of the 12th USENIX conference on Operating Systems Design and Implementation, USENIX Association, Savannah, GA, USA, 2016, pp. 265-283.
[41] Diederik P. Kingma, J. Ba, Adam: A Method for Stochastic Optimization, CoRR abs/1412.6980 (2014).
[42] A. International, ASTM D638-02 Standard Test Method for Tensile Properties of Plastics, West Conshohocken, PA, 2002.

[43] T.N. Tallman, S. Gungor, K.W. Wang, C.E. Bakis, Tactile imaging and distributed strain sensing in highly flexible carbon nanofiber/polyurethane nanocomposites, Carbon 95 (2015) 485-493.